IEEE Access
Multidisciplinary ⋮ Rapid Review ⋮ Open Access Journal

Received March 3, 2021, accepted April 10, 2021, date of publication April 20, 2021, date of current version May 11, 2021.

Digital Object Identifier 10.1109/ACCESS.2021.3074574

Accelerated Hybrid Method for Electromagnetic Scattering From Multiple Complex Targets Above a Rough Surface

GUILONG TIAN, CHUANGMING TONG, TONG WANG, AND DONGLI TANG
Air and Missile Defense College, Air Force Engineering University, Xi'an 710038, China
Corresponding author: Guilong Tian (tianguilong163@163.com)

This work was supported in part by the National Natural Science Foundation of China under Grant 61372033.

ABSTRACT A hybrid scheme that combines the pre-corrected fast Fourier transform (p-FFT) and iterative Kirchhoff approximation (IKA) is developed to solve the electromagnetic scattering from multiple complex targets above a three-dimensional (3D) rough surface. Based on the domain distribution method (DDM), multiple targets are divided into an FFT region, and the rough surface is divided into an IKA region. Scattering on the FFT region and IKA region is calculated by p-FFT and IKA, respectively. In addition, iterative strategies are considered in both solving interaction between facets in the IKA region and interactions between FFT region and IKA region. However, interactions between FFT region and IKA region are the most time-consuming in the entire computational process. To overcome this computational bottleneck, the combined multilevel fast multipole algorithm (MLFMA), ray-propagation fast multipole algorithm (RPFMA) and fast far-field approximation (FAFFA) are incorporated into interactions between FFT region and IKA region. They accelerate the matrix vector multiplication by ''interpolation –translation –anterpolation'', while their translators are different, which result in their different computation efficiencies and application conditions. To effectively combine these three algorithms, the IKA region is divided into MLFMA area, RPFMA area and FAFFA area according to the distance, where interactions between these areas and the targets are accelerated by MLFMA, RPFMA and FAFFA, and the surface outside these areas is discarded. Compared with MLFMA, the accuracy and efficiency of this hybrid method are verified.

INDEX TERMS Composite electromagnetic scattering, multiple targets above surface, accelerated technique.

I. INTRODUCTION

The composite scattering characteristics from multiple targets and rough surface are widely used in both military and civilian applications [1], [2]. In military applications, swarm operations and UAV cluster tactics are the trend of future wars. Civilian applications include multi-target identification, detection, and imaging. Xu and Guo [3] adopted FEM/BIM to compute the electromagnetic scattering from multiple objects above a 1D rough surface. Ren *et al.* [4] analyzed the electromagnetic scattering characteristic from multiple columns partially buried in a 1D ground plan by FDTD. Tian *et al.* [5] and Li *et al.* [6] computed the composite electromagnetic scattering from multiple columns above a 1D conducting rough surface based on the coupling MoM-PO. Tian *et al.* [7] presented an improved MoM-PO method to compute 3D multiple objects above a rough surface, where interactions between objects and rough surface are accelerated by FAFFA. In addition, He [8] introduced FE-BI-FMM to analyze the electromagnetic scattering from multiple simple-coating dielectric objects above a 1D rough surface. Ren [9] computed the scattering coefficient from multiple columns above a 1D rough surface with PO-PO and analyzed the scattering characteristics from multiple objects above a 2D rough surface with PO-SBR. Most articles about composite scattering from multiple targets above a rough surface concentrated on 1D rough surface with 2D multiple objects or on simple objects. In the real case of composite scattering between multiple targets and the environment, the targets are usually complex, and structures are fine, where precise calculation is required. Meanwhile, large numbers of targets request that the size of the rough surface must be sufficiently large, which results in an expensively large coupling matrix. Thus, how to promise the accuracy of computation and improve the efficiency has become a problem to solve. To solve this problem, a hybrid method [10], [11], [43], [44]

The associate editor coordinating the review of this manuscript and approving it for publication was Mehmet Alper Uslu.

that combines a numerical method and a high-frequency method is adopted. By applying the numerical method to solve for the scattering from targets due to the complex structure and the high-frequency method to compute the large-size rough surface, the hybrid numerical-analytical method promises the accuracy and efficiency for computation. Furthermore, the mesh densities are usually different for the targets and rough surface in the composite model. Thus, hybrid methods are useful to improve the instability by implementing different methods for the targets and rough surface.

The method of moment (MoM) [12] is widely used to compute electromagnetic scattering from complex targets. However, MoM is mostly applied to electric small-size problems because the computational complexity and storage requirement are extremely high for MoM. To improve the efficiency of MoM, there are two main types of algorithms: MLFMA-based algorithms [13], [14] and FFT-based algorithms [15]–[17]. In addition, PILE [41] and PILE-ACA [42] are also applied for improving the efficiency of MoM. MLFMA-based algorithms expand the integral terms, i.e., Green function, into a series with special functions as general terms according to the spherical wave addition theorem. However, due to the dependence of the series expansion of the integral kernel, the problem of sub-wavelength collapse occurs when the mesh density is high, which restricts the application of the MLFMA. The FFT-based algorithms essentially utilize the translation invariance of Green function, which is not related to the frequency and will not suffer from ''low-frequency interruption''. FFT-based algorithms include AIM, p-FFT, and IE-FFT. In AIM [15], projection coefficients are obtained by matching higher-order moments and are independent of Green function. However, numerical practice shows that AIM is only suitable for fine Cartesian grids, which makes the FFT scale relatively large. Then, Phillips and White [18] proposed the p-FFT algorithm for electrostatic problems. Unlike AIM, the projection coefficient is obtained by matching the potential function when the basis function is projected on regular grid nodes. This projection scheme enables Green function to join the process of determining the projection coefficient. Numerical practice shows that p-FFT uses a coarser Cartesian regular grid than AIM, which alleviates the pressure on FFT, and p-FFT is superior to AIM in both accuracy and flexibility [19]. Numerical practice shows that IE-FFT and AIM have identical accuracies, but both are lower than p-FFT [20].

High-frequency approximation algorithms are most used to solve scattering from electrical large rough surfaces. Kirchhoff approximation (KA) -based methods have provided engineers with a useful alternative to numerical methods to generate fast results but at the cost of decreased accuracy [21]. First-order KA includes the direct reflection and diffraction by the target from the KA approximation of the induced surface currents. Only the optically lit part of the geometry has non-zero currents, which introduces abrupt shadow boundaries that, when integrated, cause false edge diffraction effects. The strong double-bounce from the dihedral corner reflector is not included in the first-order KA. To incorporate the multiple-bounce effect, the shooting bounce racing method (SBR) [22] is considered by combining KA and GO. However, the first GO bounce causes another abrupt shadow boundary on the second surface, which also produces a false diffraction. Furthermore, the false diffractions in the SBR method can be misinterpreted as real scattering centers by target recognition algorithms [23]. Compared to the first-order KA and SBR, IKA has a slower efficiency. However, unlike other high-frequency asymptotic methods, no ray tracing is required, and spurious diffraction effects from non-physical shadow boundaries are avoided. In addition, the computational efficiency is greatly higher than numerical algorithms because the mesh density is coarser. Thus, IKA is suitable for solving the electrical large rough surface.

During the entire process to compute composite scattering, solving interactions between multiple targets and rough surface is the most difficult bottleneck. The number of targets that request a rough surface must be large, which results in an extremely large impedance matrix between targets and rough surface. However, most algorithms [5], [6], [10], [11] directly compute the interactions between targets and rough surface, which is very time-consuming. The multilevel fast multipole algorithm (MLFMA) [13] is used to accelerate the matrix vector multiplications by ''interpolation–translation–anterpolation''; it transfers the direct interaction between two groups into an interaction between two group centers and decreases the computing complexity. In MLFMA, translators are defined on the entire Ewald sphere, which must calculate all sampling directions. Research shows that when targets are near the rough surface, the direct computation is necessary because interactions between targets and rough surface are very strong [24]. However, when two groups are far away from each other, interactions between two groups gradually weaken with increasing distances. The coupling energy mainly concentrates on the main beam along the direction from the center of the source group to the center of the field group. Furthermore, the width of the main beam is linearly related to the distance: a larger distance corresponds to a narrower beam. Thus, when the distance increases, the sampling directions in the main beam are further reduced. Thus, Wrap [24] proposed the racing propagation fast multiple algorithm (RPFMA). The translators are computed with Windows function, and the width of the main beam is set. Thus, the sampling directions outside the main beam are discarded, and only few sampling directions are preserved. Furthermore, Lu and Chew [25] proposed the fast far-field approximation (FAFFA); the translator is simplified into only one sampling direction along the source group center to the field group center, when the distance satisfies the far-field condition, which effectively reduces sampling directions from $K = 2L^2+4$ to 1. Later, the FAFFA was extended to a 3D case in [26]. However, the proposed FAFFA is not sufficiently efficient because many groups cannot satisfy the far-field condition and are directly computed. To solve the

matrix vector multiplications in the near region, the combined FAFFA with MLFMA is proposed [27], [28]. Regrettably, FAFFA-MLFMA is not easily error-controllable [29]. In this paper, MLFMA and RPFMA with FAFFA are first combined to accelerate the matrix vector multiplication between targets and rough surface. Then, the rough surface is divided into different areas and solved by MLFMA, RPFMA and FAFFA.

In addition, in our previous article [45], an improved coupled MoM-PO is presented, where, the scattering of the rough surface is taken as a part of the target impedance matrix, and the target and the rough surface are solved as a whole. Among them, the rough surface scattering is calculated by the first-order Kirchhoff approximation, the target impedance matrix is accelerated by AIM, and the coupling between the target and the rough surface is accelerated by MLFMA-FAFFA. Based on our previous work, this article has a great improvement in many aspects. First of all, this paper use iterative method, interaction between targets and rough surface are solved iteratively. Secondly, this paper uses IKA to calculate the scattering of rough surfaces. Unlike the first-order KA algorithm, the IKA method fully considers the coupling effect between the surface elements, so they have higher accuracy. At the same time, for solving the impedance matrix of the MoM part, this paper uses the p-FFT instead of AIM to solve the problem. p-FFT and AIM are both FFT-based algorithms and have basically similar calculation principles, while p-FFT is more accurate and efficient than AIM. Thirdly, for the coupling and interaction between the target and the environment, this article uses MLFMA-RPFMA-FAFFA to accelerate matrix vector multiplication. Compared with MLFMA-FAFFA, MLFMA-RPFMA-FAFFA has better iterative convergence performance.

The paper is organized as follows: p-FFT/IKA is discussed in Section II, the acceleration techniques are provided in Section III, the numerical results are presented in Section IV, and the conclusions are finally shown.

II. P-FFT/IKA HYBRID METHOD

A. P-FFT FOR SCATTERING FROM THE FFT REGION

The electric field integral equation (EFIE) [31] to conduct objects can be expressed as

$$\boldsymbol{E}^i(\boldsymbol{r})\Big|_{\tan} = jk_0\eta_0\left[\int_{\partial\Omega}(\boldsymbol{J}(\boldsymbol{r'})+\frac{\nabla\nabla'\cdot}{k_0^2}\boldsymbol{J}(\boldsymbol{r'}))G(\boldsymbol{r},\boldsymbol{r'})ds'\right]_{\tan} \quad (1)$$

where $\boldsymbol{E}^i(\boldsymbol{r})$ is the outer incident electric field, $\boldsymbol{J}(\boldsymbol{r'})$ is the electric current on the surface of the object, k_0 is the wave number, and η_0 is the wave impedance. $G(\boldsymbol{r},\boldsymbol{r'})$ is Green function in the free space. Rao-Wilton-Glisson (RWG) [32]function is selected as the testing function, and the matrix function can be expressed as

$$\boldsymbol{ZI} = \boldsymbol{V} \quad (2)$$

Impedance matrix $\boldsymbol{Z}$ can be divided into near-field and far-field parts

$$\boldsymbol{Z} = (\boldsymbol{Z} - \boldsymbol{Z}^{\text{far}}) + \boldsymbol{Z}^{\text{far}} \approx \boldsymbol{Z}^{\text{near}} + \boldsymbol{Z}^{\text{far}} \quad (3)$$

where near-zone matrix $\boldsymbol{Z}^{\text{near}}$ is a sparse matrix obtained by setting the "far element" in $\boldsymbol{Z} - \boldsymbol{Z}^{\text{far}}$ to be zero, and far-zone matrix $\boldsymbol{Z}^{\text{far}}$ can be expressed as [16]

$$\boldsymbol{Z}^{\text{far}} = \boldsymbol{V}_m^T\boldsymbol{H}\boldsymbol{W}_n \quad (4)$$

where $\boldsymbol{W}$ is a projection operator to project the element source distributions to point sources on the uniform grid; $\boldsymbol{H}$ is the convolution operator to compute the potentials at the grid point due to the grid sources by FFT-accelerated convolutions; $\boldsymbol{V}$ is the interpolation operator to interpolate the grid-point potentials onto the elements. The detailed definitions of $\boldsymbol{W}$, $\boldsymbol{H}$ and $\boldsymbol{V}$ are in [16], [19], [30].

The pre-correction operator is [16]

$$\boldsymbol{P}(m,n) = \boldsymbol{Z}(m,n) - \boldsymbol{Z}^{FFT}(m,n) \quad (5)$$

After applying the four operators of the p-FFT method, the p-FFT approximation of $\boldsymbol{Z}_{mn}$ is

$$\boldsymbol{Z}^{p-FFT}(m,n) = \boldsymbol{P}(m,n) + \boldsymbol{V}_m^T\boldsymbol{H}\boldsymbol{W}_n \quad (6)$$

We suppose that the number of basic functions is N_{b}, and the number of grids is N_{g}. Thus, after applying the p-FFT method, the impedance matrix of (6) can be converted into

$$\boldsymbol{Z}_{N_b\times N_b}\boldsymbol{I}_{N_b\times 1} = \boldsymbol{P}_{N_b\times N_b}\boldsymbol{I}_{N_b\times 1} + \boldsymbol{V}_{N_b\times N_g}\boldsymbol{H}_{N_g\times N_g}\boldsymbol{W}_{N_g\times N_b}\boldsymbol{I}_{N_b\times 1} \quad (7)$$

B. IKA FOR SCATTERING FROM THE IKA REGION

Based on the first-order Kirchhoff approximation, the induced currents on the rough surface can be expressed as

$$\boldsymbol{J} = 2\hat{n}\times\boldsymbol{H}^i \quad (8)$$

where $\hat{n}$ is the unit outer normal vector of a rough surface; $\boldsymbol{H}^i$ is the outer incident magnetic field; $\boldsymbol{J}$ is the induced currents on the rough surface. Based on the surface magnetic field integral equation (MFIE) [33] on the rough surface, we consider the scattering field excited by electric currents $\boldsymbol{J}$ and magnetic currents $\boldsymbol{M}$ on the rough surface, and the induced currents can be rewritten as

$$\boldsymbol{J} = 2\hat{n}\times\boldsymbol{H}^i + 2\hat{n}\times L(\boldsymbol{M}) + 2\hat{n}\times K(\boldsymbol{J}) \quad (9)$$

where the expression of $L(\boldsymbol{M})$ and $K(\boldsymbol{J})$ are

$$\begin{aligned} L(\boldsymbol{M}) &= \iint_s -j\omega\varepsilon_0[\boldsymbol{M}(\boldsymbol{r'})g(\boldsymbol{r},\boldsymbol{r'}) + \frac{1}{k^2}\nabla' \\ &\quad \cdot\boldsymbol{M}(\boldsymbol{r'})\nabla g(\boldsymbol{r},\boldsymbol{r'})]ds' \\ K(\boldsymbol{J}) &= \iint_s \boldsymbol{J}(\boldsymbol{r'})\times\nabla g(\boldsymbol{r},\boldsymbol{r'})ds' \end{aligned} \quad (10)$$

ω is the angular frequency; ε_0 is the relative dielectric constant; k is the propagation constant in free space; $g(\boldsymbol{r},\boldsymbol{r'})$ is Green function in free space. Subscript s denotes the entire rough surface. When the rough surface satisfies the impedance boundary condition [34] $\boldsymbol{M} = \boldsymbol{Z}_S\boldsymbol{J}\times\hat{n}$ ($\boldsymbol{Z}_s = \eta_0/\sqrt{\varepsilon_r}$), Eq.(9) can be rewritten as [39]

$$\boldsymbol{J} = 2\hat{n}\times\boldsymbol{H}^i + 2Z_S\hat{n}\times L(\boldsymbol{J}\times\hat{n}) + 2\hat{n}\times K(\boldsymbol{J}) \quad (11)$$

The induced currents on facet i are

$$\boldsymbol{J}_i = 2\hat{n}_i \times \boldsymbol{H}^i + \sum_{j=1,j\neq i}^{N} Y_{ij}(\boldsymbol{J}_j, Z_S) \tag{12}$$

where $Y_{ij}(.)$ denotes the composite integral from facet j and can be expressed as

$$Y_{ij}(\boldsymbol{J}_j, Z_S) = 2Z_S\hat{n}_i \times L(\boldsymbol{J}_j \times \hat{n}_i) + 2\hat{n}_i \times K(\boldsymbol{J}_j) \tag{13}$$

The initial value of electric currents is set as $\boldsymbol{J}^{(0)} = 2\hat{n} \times \boldsymbol{H}^i$, and Eq. (12) can be rewritten as

$$\boldsymbol{J}_i^{(n+1)} = \boldsymbol{J}_i^{(0)} + \sum_{j=1,j\neq i}^{N} Y_{ij}(\boldsymbol{J}_j^{(n)}, Z_S) \tag{14}$$

By implementing the forward and backward iterative method (FBM) [35], the electrics and magnetics on the rough surface are obtained.

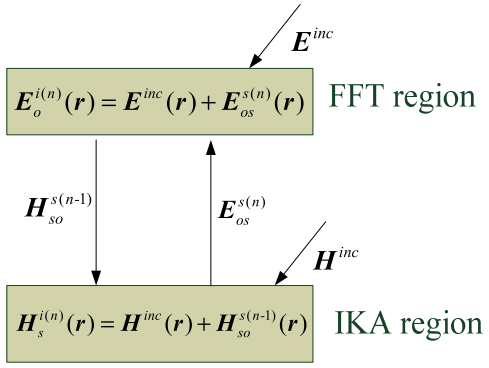

FIGURE 1. Schematicof interaction between FFT region and IKA regio.

C. INTERACTIONS BETWEEN FFT REGION AND IKA REGION

As we see in figure.1, the interaction process between FFT region and IKA region at the *n-th* step can be expressed as

$$\begin{aligned} \boldsymbol{H}_s^{i(n)}(\boldsymbol{r}) &= \boldsymbol{H}^{inc}(\boldsymbol{r}) + \boldsymbol{H}_{so}^{s(n-1)}(\boldsymbol{r}), \quad \boldsymbol{r} \in S_s \\ \boldsymbol{E}_o^{i(n)}(\boldsymbol{r}) &= \boldsymbol{E}^{inc}(\boldsymbol{r}) + \boldsymbol{E}_{os}^{s(n)}(\boldsymbol{r}), \quad \boldsymbol{r} \in S_o \ (n = 1, 2, ...) \end{aligned} \tag{15}$$

where $\boldsymbol{H}_s^{i(n)}$ and $\boldsymbol{E}_o^{i(n)}$ are the total excitation field on the IKA region and FFT region, respectively; $\boldsymbol{E}^{inc}$ and $\boldsymbol{H}^{inc}$ are the incident electric and magnetic fields, respectively; $\boldsymbol{H}_{so}^{s}$ is the interaction magnetic field that the induced electric currents on the targets impact on the rough surface; $\boldsymbol{E}_{os}^{s}$ is the interaction electric field that the induced electromagnetic current on the rough surface impacts on the targets. Interaction fields $\boldsymbol{H}_{so}^{s}$ and $\boldsymbol{E}_{os}^{s}$ at the n-th iteration can be expressed as

$$\begin{aligned} \boldsymbol{H}_{so}^{s(n-1)}(\boldsymbol{r}) &= \iint_{s_o} \boldsymbol{J}_o^{(n-1)}(\boldsymbol{r}') \times \nabla g(\boldsymbol{r}, \boldsymbol{r}') ds' \\ \boldsymbol{E}_{os}^{s(n)}(\boldsymbol{r}) &= \iint_{s_s} \{-j\omega\mu_0[\boldsymbol{J}_s^{(n)}(\boldsymbol{r}')g(\boldsymbol{r}, \boldsymbol{r}') \\ &\quad + \frac{1}{k^2}\nabla' \cdot \boldsymbol{J}_s^{(n)}(\boldsymbol{r}')\nabla g(\boldsymbol{r}, \boldsymbol{r}')] \\ &\quad + \boldsymbol{M}_s^{(n)}(\boldsymbol{r}') \times \nabla g(\boldsymbol{r}, \boldsymbol{r}')\} ds' \end{aligned} \tag{16}$$

where $\boldsymbol{J}_o$ is the induced electric current in the FFT region; $\boldsymbol{J}_s$ and $\boldsymbol{M}_s$ are the induced electric current and magnetic current in the IKA region, respectively. By updating the excitation item on the left of Eq. (15), substituting the updated $\boldsymbol{E}_o^{i(n)}$ into Eq. (1) as the outer incident electric field and the updated $\boldsymbol{H}_s^{i(n)}$ into Eq. (12) as outer incident magnetic field, and updating the induced electromagnetic current in the FFT region and IKA region, we obtain the electric current and magnetic current.

The iteration error at the *n-th* step is

$$\xi_o^{(n)} = \frac{||\boldsymbol{J}_o^{(n+1)} - \boldsymbol{J}_o^{(n)}||_2}{||\boldsymbol{J}_o^{(n)}||_2}, \quad \xi_s^{(n)} = \frac{||\boldsymbol{J}_s^{(n+1)} - \boldsymbol{J}_s^{(n)}||_2}{||\boldsymbol{J}_s^{(n)}||_2} \tag{17}$$

where $\xi_o^{(n)}$ and are the iteration errors of the electric current on the targets and on the rough surface, respectively. The convergence threshold of the iteration error is set as 10^{-3}, where the induced electric current and magnetic current should be stable, and the iteration process will stop. Finally, the electric current and magnetic current are obtained.

In fact, the computation of the coupling fields $\boldsymbol{H}_{so}^{s}$ and $\boldsymbol{E}_{os}^{s}$ is the most difficult computational bottleneck in the composite scattering computation from multiple targets above a rough surface. On one hand, the coupling impedance matrix element does not preserve in each iteration step, which decreases the storage requirement. On the other hand, after the induced currents in the former iteration are obtained, the coupling fields $\boldsymbol{H}_{so}^{s}$ and $\boldsymbol{E}_{os}^{s}$ must be computed again, and the matrix vector multiplication between FFT region and IKA region will consume enormous computing resource. To overcome this bottleneck, an efficient acceleration technique that combines the MLFMA, RPFMA and FaFFA is used to accelerate the matrix vector multiplication.

III. ACCELERATION TECHNIQUE

A. MLFM

An oct-tree structure is defined to implement MLFMA; the size of final boxes is approximately 0.5 λ. Suppose that $\boldsymbol{r}_m$ and $\boldsymbol{r}_{m'}$ are the center vectors of the field group and source group, respectively. $\boldsymbol{r}_a$ and $\boldsymbol{r}_b$ are the field point and source point, and $\boldsymbol{r}_{ab} = \boldsymbol{r}_a - \boldsymbol{r}_b = \boldsymbol{r}_{mm} = \boldsymbol{r}_{mm'} - \boldsymbol{r}_{bm'}$. When the distance satisfies the condition $|\boldsymbol{r}_{mm'}| > |\boldsymbol{r}_{am} - \boldsymbol{r}_{bm'}|$, the scalar Green function can be expressed as [36]

$$\frac{e^{-jk_0|r_a - r_b|}}{|\boldsymbol{r}_a - \boldsymbol{r}_b|} = \frac{ik_0}{4\pi}\int_{S_E} d^2\hat{k} e^{ik_0\hat{k}.(r_{am} - r_{bm'})}\alpha_{mm'}(\hat{k}.\hat{r}_{mm'}) \tag{18}$$

where $\int d^2\hat{k}$ denotes the integral on the unit sphere S_E of the spectrum space. $\alpha_{mm'}(\hat{k}.\hat{r}_{mm'}$ is the translator from the center of the field group to the center of the source group and can be expressed as [28]

$$\alpha_{mm'}(\hat{k} \cdot \hat{r}_{mm'}) = \sum_{l=0}^{L}(-j)^l(2l+1)h_l^{(1)}(k_0 r_{mm'})P_l(\hat{k} \cdot \hat{r}_{mm'}) \tag{19}$$

where $j_l(kd)$ is the spherical Bessel function of the first type; h_l^1 is the spherical Hankel function of the first type; P_l is

Legendre polynomial; L is the truncation number of infinite summation; $L = kD + \beta(kD)^{1/3}$ [37]. The total sampling number of $\hat{k}$ on the Ewald sphere is [29]: $K = 2L^2 + 4$. Apparently, the total sampling number is enormous. It consumes a large quantity of computation resource to perform the translation in MLFMA. The gradient of Green function is

$$\nabla \frac{e^{ik_0|r_a - r_b|}}{|\boldsymbol{r_a} - \boldsymbol{r_b}|} = \frac{k}{4\pi} \int_{S_E} d^2\hat{k} e^{i\boldsymbol{k}.(\boldsymbol{r}_{am} - \boldsymbol{r}_{bm'})} \alpha(\hat{k}.\hat{\boldsymbol{r}}_{mm'}) \tag{20}$$

B. RPFMM

Ref. [24] shows that only $\hat{k}$ vectors around ray direction $\boldsymbol{r}_{mn}$ really greatly contribute to the interaction, and this form constitutes the RPFMA [24]. To successfully perform the RPFMA, a window function is introduced to smooth the transition from one to zero. Thus, Eq. (19) can be rewritten as [29]

$$\alpha_{mm'}(\hat{k} \cdot \boldsymbol{r}_{mm'}) = \sum_{l=0}^{L} (-j)^l (2l+1) h_l^{(1)}(kr_{mm'}) P_l(\hat{k} \cdot \hat{r}_{mm'}) \omega_l \tag{21}$$

where ω_l is [38]

$$\boldsymbol{W}_l = \begin{cases} 1 & l \le J \\ 0.5\{1 + \cos[\dfrac{(l-J)\pi}{(L-J)}]\} & l > J \end{cases} \tag{22}$$

where J varies with the number of layers; for the finest level, J is equal to 0.8L; for the second level, J is equal to 0.4L; the middle layer linearly decreases from $0.8L$ to $0.4L$ [38], which realizes the tapering of the translator, i.e., the angular spectrum main beam direction is more prominent, and the contribution of the angular spectrum in other directions decreases with the increase in angle between it and the main beam.

C. FAFFA

When the group distance satisfies the far-field condition, the translator can be simplified by using FAFFA where only a single $\hat{k}$ is involved in the translator along the ray-propagation direction. The translator can be simplified as [29]

$$\alpha_{mn}^{far} = 4\pi \frac{e^{ikr_{mn}}}{ikr_{mn}} \delta(\hat{k} - \hat{r}_{mn}) \tag{23}$$

Here, we show that only one sampling direction is involved in the FAFFA translator along the ray-propagation direction from group m to group n, and the condition for FAFFA must satisfy [13]

$$r_{mn} \ge 3\gamma \sqrt{(D_x^l)^2 + (D_y^l)^2 + (D_z^l)^2} \tag{24}$$

where $3\sqrt{(D_x^l)^2 + (D_y^l)^2 + (D_z^l)^2}$ is the maximum distance of two groups in the second nearest neighbors, and $\gamma \ge 1$. Furthermore, the coarsest level L_C should satisfy $L_C > 2$.

D. COMBINATION OF MLFM, RPFMA AND FAFFA

By substituting Eq. (18) and (20) into Eq. (16), we obtain

$$\begin{aligned}
&\boldsymbol{H}_{s_i o}^{s(n+1)} \\
&= \sum_{o_j \in N_m} \boldsymbol{H}_{s_i o_j}^{(n)} + \int_{S_E} d^2\hat{k} \boldsymbol{V}_{fmi}^{(s)}(\hat{k}) \sum_{m' \in M_m} \alpha(\hat{k} \cdot \hat{r}_{mm'}) \sum_{o_j \in G_{m'}} \boldsymbol{V}_{sm'j}^{(o)}(\hat{k}) \\
&\quad + \int_{RS_E} d^2\hat{k} \boldsymbol{V}_{fmi}^{(s)}(\hat{k}) \sum_{m' \in R_m} \alpha^R(\hat{k} \cdot \hat{r}_{mm'}) \sum_{o_j \in G_{m'}} \boldsymbol{V}_{sm'j}^{(o)}(\hat{k}) \\
&\quad + \int_{FS_E} d^2\hat{k} \boldsymbol{V}_{fmi}^{(s)}(\hat{k}) \sum_{m' \in F_m} \alpha^F(\hat{k} \cdot \hat{r}_{mm'}) \sum_{o_j \in G_{m'}} \boldsymbol{V}_{sm'j}^{(o)}(\hat{k}) \\
&\boldsymbol{E}_{o_i s}^{(n)} \\
&= \sum_{s_j \in N_m} \boldsymbol{E}_{o_i s_j}^{(n)} + \int_{S_E} d^2\hat{k} \boldsymbol{V}_{fmi}^{(o)}(\hat{k}) \sum_{m' \in M_m} \alpha(\hat{k} \cdot \hat{r}_{mm'}) \sum_{s_j \in G_{m'}} U_{sm'j}^{(s)}(\hat{k}) \\
&\quad + \int_{RS_E} d^2\hat{k} \boldsymbol{V}_{fmi}^{(o)}(\hat{k}) \sum_{m' \in R_m} \alpha^R(\hat{k} \cdot \hat{r}_{mm'}) \sum_{s_j \in G_{m'}} U_{sm'j}^{(s)}(\hat{k}) \\
&\quad + \int_{FS_E} d^2\hat{k} \boldsymbol{V}_{fmi}^{(o)}(\hat{k}) \sum_{m' \in F_m} \alpha^F(\hat{k} \cdot \hat{r}_{mm'}) \sum_{s_j \in G_{m'}} U_{sm'j}^{(s)}(\hat{k})
\end{aligned} \tag{25}$$

where

$$\begin{aligned}
\boldsymbol{V}_{fmi}^{(o)}(\hat{k}) &= -\frac{jk_0}{4\pi} e^{-j\boldsymbol{k} \cdot \boldsymbol{r}_{im}^{(o)}} \\
\boldsymbol{V}_{fmi}^{(s)}(\hat{k}) &= -\frac{jk_0}{4\pi} e^{-j\boldsymbol{k} \cdot \boldsymbol{r}_{im}^{(s)}} \\
\boldsymbol{V}_{sm'j}^{(o)}(\hat{k}) &= \int_s (\hat{k} \times \boldsymbol{J}_{o_j}^{(n)}) e^{j\boldsymbol{k} \cdot \boldsymbol{r}_{jm'}^{(o)}} ds' \\
U_{sm'j}^{(s)}(\hat{k}) &= \int_s [\hat{k} \times \boldsymbol{M}_{s_j} - j\omega\mu_0 \boldsymbol{J}_{s_j} \cdot (\bar{\bar{I}} - \hat{k}\hat{k})] e^{j\boldsymbol{k} \cdot \boldsymbol{r}_{jm'}^{(s)}} ds'
\end{aligned} \tag{26}$$

$G_{m'}$ is the source group m'; M_m is the MLFMA area; R_m is the RPFMA area; F_m is the FAFFA area; S_E is the integral area on the entire Ewald sphere; RS_E is the integral area on Ewald sphere defined by RPFMA; FS_E is the integral area on Ewald sphere defined by FAFFA; $V_{fmi}^{(o)}$ and $V_{fmi}^{(s)}$ are anterpolations in the FFT region and IKA region, respectively; $V_{sm'j}^{(o)}$ and $U_{sm'j}^{(s)}$ are interpolations in the FFT region and IKA region, respectively; $\alpha(\cdot)$, $\alpha^R(\cdot)$ and $\alpha^F(\cdot)$ are translators defined by MLFMA, RPFMA and FAFFA, respectively.

According to Eq. (22) and (24), the FFT region is divided into the MLFMA area, RPFMA area and FAFFA area. Furthermore, when rough surface becomes sufficiently large, the electromagnetic coupling between targets and rough surface weakens with the increase in distance, and the increase in radiated area of the surface will not make a new electromagnetic contribution to difference field radar cross section(d-RCS). Thus, the size of the FFT region can be further truncated according to Ref. [39]

$$\begin{aligned}
L_x &\ge 2z_{\max} \sqrt{\xi^{-4/3} - 1} + L_{ox} \\
L_y &\ge 2z_{\max} \sqrt{\xi^{-4/3} - 1} + L_{oy}
\end{aligned} \tag{27}$$

where ξ is the error parameter; $\xi \leq 0.01$; $z_{\max}$ is the height of the targets above the rough surface; L_{ox} and L_{oy} are the maximum projection distances on the X axis and Y axis.

IV. NUMERICAL RISULTS AND ANALYSIS

A. VERIFICATION

In the following examples, the working frequency is $f = 1$ GHz; the incident angle is $\theta_i = 30°$. The rough surface is simulated by Gaussian spectrum; the size of the rough surface is $L_x \times L_y = 50\lambda \times 50\lambda$; 10 sampling points are considered per wave length, the root mean square (RMS) height of the rough surface is $\boldsymbol{h}_r = 0.1\lambda$, the correlation length of the rough surface is $l_x = l_y = 4.0\lambda$. The computing platform is an Intel(R) processor of 2.6 GHz with 64 kernels and 192 GB RAM. The examples in the paper calculate the statistic average of 30 rough surfaces generated by Monte Carlo method. In this paper, a tapered incident beam is introduced in order to circumvent artificial truncation effects [40], and the 3D form of it is given by

$$E^{inc} = G(x, y, z) \cdot \exp[-jk_0(\cos\theta_i z - x\sin\theta_i \cos\varphi_i - y\sin\theta_i \sin\varphi_i)] \quad (28)$$

where

$$G(x, y, z) = \exp[-jk_0(\cos\theta_i z - x\sin\theta_i \cos\varphi_i - y\sin\theta_i \sin\varphi_i)w(x,y,z)] \exp(-t_x - t_y) \quad (29a)$$

$$t_x = (\cos\theta_i \cos\varphi_i x + \cos\theta_i \sin\varphi_i + \sin\varphi_i z)^2 / (g_x^2 \cos^2\theta_i) \quad (29b)$$

$$t_x = (-\sin\varphi_i x + \cos\varphi_i y)^2 / g_y^2 \quad (29c)$$

$$w(x, y, z) = [(2t_x - 1)/(g_x^2 \cos^2\theta_i) + (2t_y - 1)/g_y^2]/k_0^2 \quad (29d)$$

where, the factor of beam width in x and y direction are set as $g_x = L_x/4$, $g_y = L_y/4$.

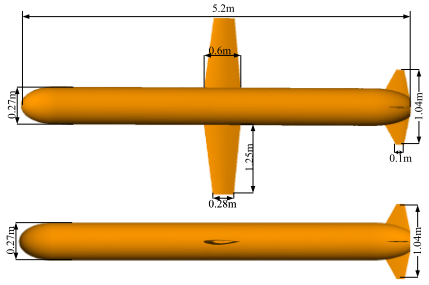

FIGURE 2. Geometry of the missile-like targe.

The size of missile-like targets is shown in figure. 2, and the geometry of two missile-like targets above the rough surface is shown in figure. 3. The altitude of the target from the underlying rough surface is H = 10λ. The comparing results of p-FFT/IKA-MLFMA/RPFMA/FAFFA with MLFMA from two missile-like targets above the underlying rough surface with different RMS are presented in figure.4 and figure. 5.

As we see, both in RMS is 0.1λ and RMS is 0.3λ, the accelerated p-FFT/IKA have good agreement with MLFMA. And

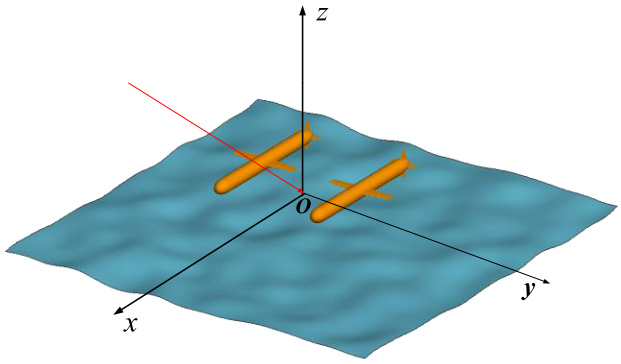

FIGURE 3. Geometry of wo missile-like targets above the rough surface.

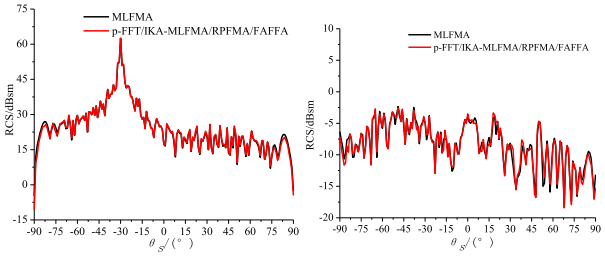

FIGURE 4. Comparison of RCS obtained by p-FFT/IKA-MLFMA/RPFMA/FAFFA and MLFMA with RMS is $h_r = 0.1$ λ (a) VV polarization, (b)VH polarization.

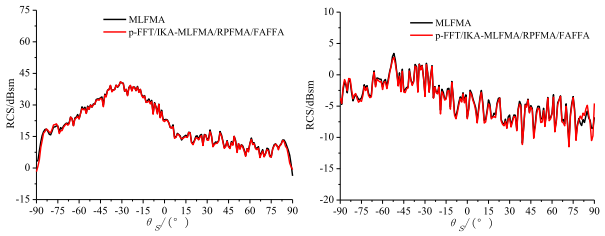

FIGURE 5. Comparison of RCS obtained by p-FFT/IKA-MLFMA/RPFMA/FAFFA and MLFMA with RMS is $h_r = 0.3$ λ (a)VV polarization, (b)VH polarization.

with RMS increasing, the specular scattering gets weak and the backward scattering get stronger. In addition, RCS for VH polarization increases with RMS increases. The reasons are that with RMS increase, the incoherent scattering get stronger while the coherent scattering gets weak, and the radio scatting is mainly caused by coherent scattering while the backward scattering is mainly caused by in coherent scattering.

To better analyze the accuracy of the proposed method, the function of error analysis is used, and the expressions of mean deviation and max deviation are

$$\langle\gamma\rangle = \frac{1}{N_{\theta_s}} \sum_{\{\theta_s\}} |\gamma^T(\theta_s) - \gamma^M(\theta_s)| \quad (30)$$

$$\max\gamma = \max_{\{\theta_s\}} |\gamma^T(\theta_s) - \gamma^M(\theta_s)| \quad (31)$$

where $\gamma^T(\theta_s)$ is the BCS obtained by improved MoM-PO, $\gamma^M(\theta_s)$ is the BCS obtained by the MoM, and N_{θ_s} is the number of scattering angles.

TABLE 1. Error analysis for different conditions.

RMS	Polarizations	$\langle\gamma\rangle$/dB	max γ /dB
0.1λ	VV	0.3293	1.7094
	VH	0.4755	2.1561
0.3λ	VV	0.3975	2.3519
	VH	0.4832	2.5965

TABLE 2. Comparison of the computation results and storage requirement by two solvers.

Polarization model	Method	Computation time/h	Storage requirement/Gbyte
0.1λ	MLFMA	8.335	37.727
	Accelerated p-FFT/IKA	5.2905	15.52
0.3λ	MLFMA	10.596	37.957
	Accelerated p-FFT/IKA	6.221	15.96

The comparison results of error analysis are shown in TABLE 1. As we see, for both the RMS is $h_r = 0.1\lambda$ and RMS is $h_r = 0.3\lambda$, the accelerated p-FFT/TKA has good agreement with MLFMA. The reasons are that p-FFT is an accurate numerical method, and IKA have considered the mutual interactions between different facets of rough surface, thus p-FFT/IKA have good accuracy.

The comparison results of the computation time and storage requirements are shown in TABLE 2. As we see, the computing time of p-FFT/IKA-MLFMA/RPFMA/FAFFA is about 60% of MLFMA, and the storage requirement is about 41% of MLFMA. Thus, p-FFT/IKA-MLFMA/RPFMA/FAFFA is of high efficiency and low storage requirement.

B. RCS FROM DIFFERENT QUANTITIES OF TARGETS ABOVE THE ROUGH SURFACE

The comparison results of RCS from one, three, and five target/targets above a rough surface are presented in Figs.6-7. The incident angle is $\theta_i = 30°, \varphi_i = 0°$; the observation angle is $\theta_s = -90\sim90°$, $\varphi_s = 0°$. Targets are parallel to each other side by side. The height of the targets above the rough surface is 2 m. For different polarizations, when the number of targets

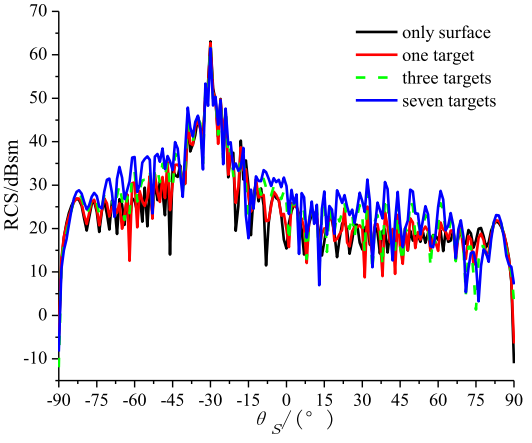

FIGURE 6. RCS for different numbers of targets in the VV polarization.

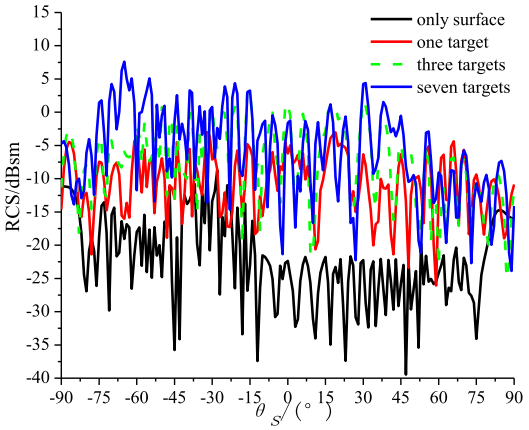

FIGURE 7. RCS for different numbers of targets in the VH polarization.

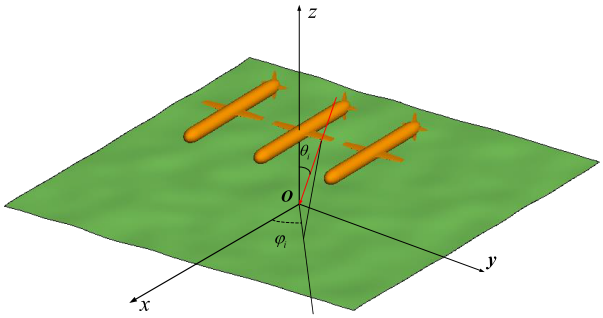

FIGURE 8. Illustration of different incident angle.

increases, RCS becomes stronger. For the VV polarization, the total RCS is stronger. For the VH polarization, in all scattering directions, more targets correspond to greater RCS, and the difference is very apparent. This result can be explained as follows: with more targets, the mutual interaction among different targets and interactions between targets and rough surface strengthen.

C. COMPOSITE SCATTERING FROM TARGETS ABOVE A ROUGH SURFACE WITH DIFFERENT INCIDENT AZIMUTH ANGLES

The comparison of the obtained RCS with different incident angles is presented in Figs.9-10. The incident angles are $\theta_i = 30°$, $\varphi_i = 0°$; $\theta_i = 30°$, $\varphi_i = 30°$; and $\theta_i = 30°$, $\varphi_i = 60°$, and the observation angles are $\theta_s = -90°\sim90°$, $\varphi_s = 0°$. The number of targets is 3, and the targets are parallel to each other side by side. For the VV polarization, RCS for the incident direction of $\varphi_i = 0°$ is the largest, and RCS decreases with the increase in azimuth angle; in addition, when the azimuth angle increases, the maximum scattering direction angle increases. For the VH polarization, when the incident azimuth angle is 0°, RCS is the smallest and relatively strong at other angles, and the maximum scattering direction angle increases with the increase in azimuth angle. The reasons are that when the azimuth angle increases, the included angle between reflection direction and receiving direction increases, so the primary reflection peak projected to the receiving direction decreases; thus, RCS decreases,

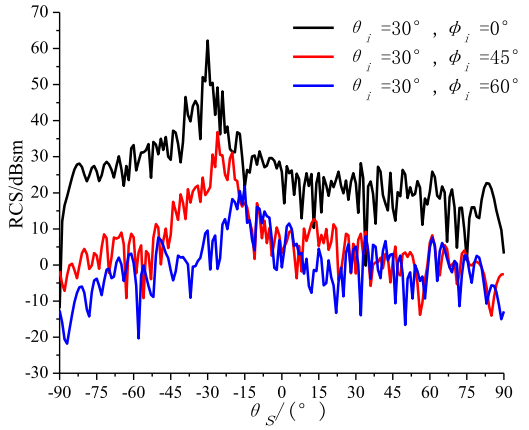

FIGURE 9. RCS for different incident angles for the VV polarization.

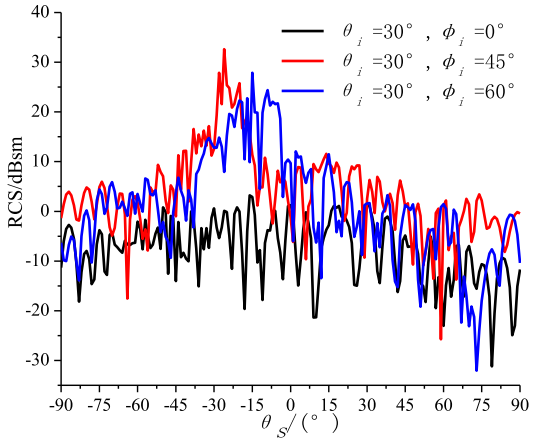

FIGURE 10. RCS for different incident angles for the VH polarization.

and the scattering angle increases. For the VH polarizations, since the wave propagation direction is perpendicular to the incident direction, RCS for the incident angle of $\varphi_i = 0°$ is minimal.

D. COMPOSITE SCATTERING FROM TARGETS ABOVE A ROUGH SURFACE WITH DIFFERENT INCIDENT PITCH ANGLES

The comparison of the obtained RCS with different incident pitch angles is presented in Figs.11-12. The incident angles are $\theta_i = 30°$, $\varphi_i = 0°$; $\theta_i = 45°$, $\varphi_i = 0°$; and $\theta_i = 60°$, $\varphi_i = 0°$, and the observation angles are $\theta_s = 30°$, $\varphi_s = 0°\sim360°$; $\theta_s = 45°$, $\varphi_s = 0°\sim360°$; $\theta_s = 60°$, $\varphi_s = 0°\sim360°$. The number of targets is 3, and the targets are parallel to each other side by side. As we see, no matter for the VV polarization or VH polarization, when the incident angle is $\theta_i = 30°$, $\varphi_i = 0°$, RCS is the largest. And when the incident angle is $\theta_i = 60°$, $\varphi_i = 0°$,RCS is the smallest. The reasons are that when incident angle is $\theta_i = 30°$, $\varphi_i = 0°$, the angle between the incident wave and the normal vector of the rough surface is the smallest, thus the incident energy is the strongest and the mutual interactions between targets and rough surface is strongest. Similarly, when the incident angle is $\theta_i = 60°$, $\varphi_i = 0°$, the mutual interactions between targets and rough surface is smallest.

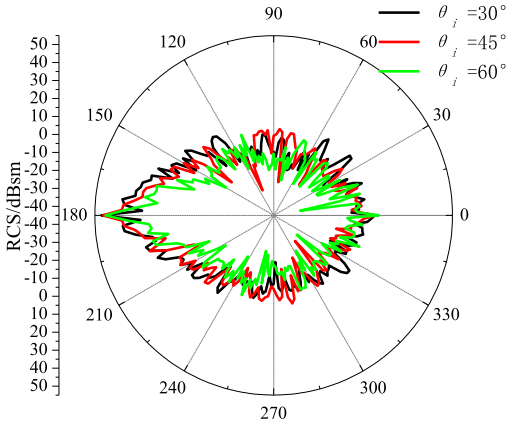

FIGURE 11. RCS for different pitch incident angles for the VV polarization.

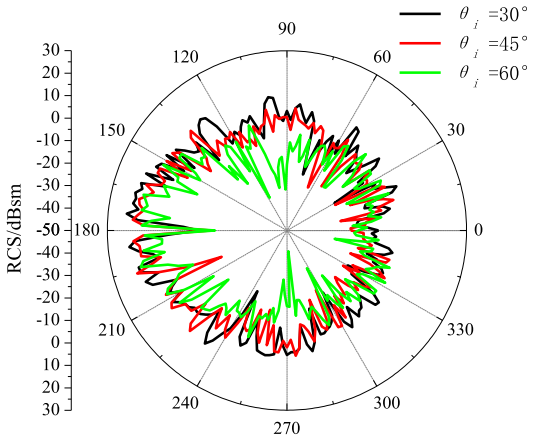

FIGURE 12. RCS for different pitch incident angles for the Hpolarization.

E. COMPOSITE SCATTERING FROM TARGETS WITH DIFFERENT POSITIONS ABOVE A ROUGH SURFACE

The model of targets with different positions above the rough surface is shown in figure.13. The RCS results from targets with different locations above a rough surface are compared in Figs. 14-15. The incident angle is $\theta_i = 30°$, $\varphi_i = 0°$; the observation angle is $\theta_s = 30°$, $\varphi_s = 0°\sim360°$. For the VV polarizations, the radial scattering direction centered at 180° is maximal, mainly concentrates in the angle range

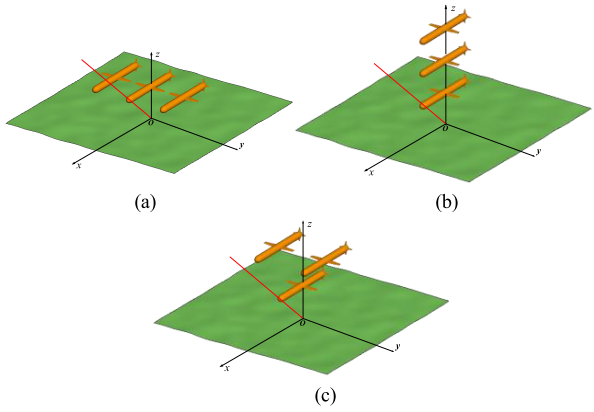

FIGURE 13. Different position of the targets above the rough surface. (a) position; (b) position; (c) position 3.

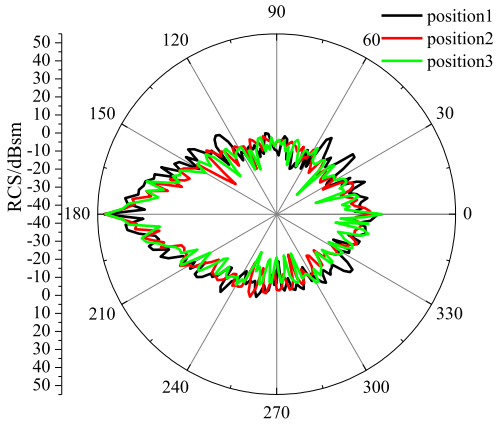

FIGURE 14. RCS for different positions for the VV polarization.

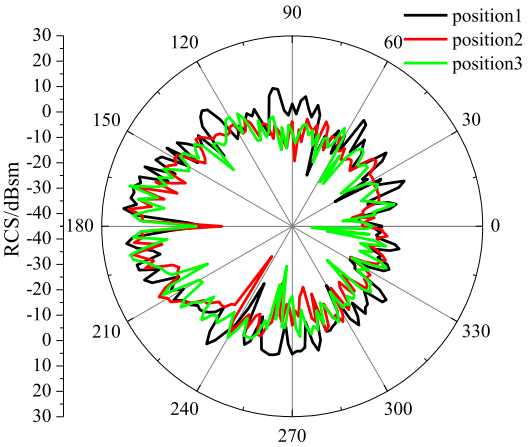

FIGURE 15. RCS for different positions for the VH polarization.

of 120° −240°, and decreases to both sides with 180° as the center. In addition, RCS in the backward scattering direction is relatively strong, mainly concentrates between −30° and 30°, and laterally decreases with 0° as the center. In the direction of $\varphi_i = 90°$ or $\varphi_i = 270°$, RCS is minimal; however, for the VH polarization, in the mirror scattering direction at 180° or backward scattering direction at 0°, RCS is the lowest. When the targets are at position 2 or position 3, RCS is relatively lower; when the targets are at position 1, RCS is relatively stronger in most scattering directions. The reasons are that the coupling energy for VV polarization is mainly concentrated in the radial scattering and backward scattering directions, so RCS in these directions is relatively strong, while RCS in the scattering direction vertical to the incident direction is weak. Moreover, due to the mirror reflection effect of the targets, RCS in radial scattering is maximal. For cross polarization, since the wave propagation direction is perpendicular to the incident direction, RCS is minimal in the directions of 0° and 180°, while it is relatively strong in other scattering directions. And when targets are at position 1, mutual interaction between targets with rough surface is stronger compared with other situations.

V. CONCLUSION

To solve scattering from multiple 3D conducting targets above a rough surface, a hybrid method that combines p-FFT and IKA is presented in this paper. Target scattering is solved by p-FFT, rough surface scattering is computed by IKA, and the interactions between targets and rough surface are iteratively solved. To accelerate the matrix vector multiplication, the combined MLFMA-RPFMA-FAFFA technique is applied in the iteration process. Based on the domain decomposition method, the rough surface is divided into MLFMA area, RPFMA area and FAFFA area, where the interactions between these areas and the targets are accelerated by MLFMA, RPFMA and FAFFA, respectively. Compared with MoM, this hybrid method is verified to have high efficiency and accuracy. In the end, the effects of the number of targets, incident angle and positions of targets on RCS are analyzed in detail. The results show that the number of targets, incident angle, target positions and frequency all have great influence on RCS, especially the number of targets and incident angle.

REFERENCES

[1] X. Cai, X. Gu, and W. Geyi, "Optimal design of antenna arrays focused on multiple targets," *IEEE Trans. Antennas Propag.*, vol. 68, no. 6, pp. 4593–4603, Jun. 2020.

[2] Y. Lu, C. Han, Z. He, S. Liu, and Y. Wang, "Adaptive JSPA in distributed colocated MIMO radar network for multiple targets tracking," *IET Radar, Sonar Navigat.*, vol. 13, no. 3, pp. 410–419, Mar. 2019.

[3] R.-W. Xu and L.-X. Guo, "Application of hybrid finite element-boundary integral algorithm for solving electromagnetic scattering from multiple objects over rough sea surface," *Int. J. Antennas Propag.*, vol. 2014, pp. 1–10, Jan. 2014.

[4] X.-C. Ren, Y. Zhao, P.-J. Yang, and X.-M. Zhu, "Electromagnetic scattering by multiple columns partially buried in a ground plane," *Int. J. Antennas Propag.*, vol. 2017, pp. 1–8, Jan. 2017.

[5] T. Wei, R. Xin-Cheng, and G. Li-Xin, "Study on composite electromagnetic scattering from the double rectangular cross-section columns above rough sea surface using hybrid method," *Acta Phys. Sinica*, vol. 64, no. 17, 2015, Art. no. 174101.

[6] L. Bing, M. Meng-Chen, and L. Ming-Zhu, "Hybrid algorithm for composite electromagnetic scattering from the multi-target on and above rough sea surface," *Acta Phys. Sinica*, vol. 66, no. 5, 2017, Art. no. 050301.

[7] G. Tian, C. Ming Tong, H. Liu, and P. Peng, "An improved MoM-PO hybrid method for scattering from multiple 3-D objects above the 2-D random conducting rough surface," *Electromagnetics*, vol. 39, no. 5, pp. 375–392, Jul. 2019.

[8] H. J. He, "Research on fast hybrid algorithm for composite electromagnetic scattering from rough surface and target based on FEM," Ph.D. dissertation, Dept. Ph. Radio Physic, Xidian Univ., ShangXi, China, 2019.

[9] Z. L. Ren, "PO-SBR algorithm for analysis of composite scattering and HRRP from the target and rough surface," M.S. thesis, Dept. Ph. Radio Phys., Xidian Univ., Shanxi, China, 2019.

[10] H. X. Ye and Y. Q. Jin, "A hybrid analytical-numerical algorithm for computation of scattering from a 3D PEC object above a dielectric rough surface," *Chin. J. Radio Sci.*, vol. 23, no. 6, pp. 1144–1187, 2008.

[11] W. Rui, G. L. X. Q. San-Tuan, and W. Zhen-Sen, "Hybrid method for investigation of electromagnetic scattering interaction between the conducting object and rough sea surface," *Acta Phys. Sinica*, vol. 57, no. 6, pp. 3473–3480, 2008.

[12] V. Erturk and R. G. Rojas, "Efficient computation of surface fields excited on a dielectric-coated circular cylinder," *IEEE Trans. Antennas Propag.*, vol. 48, no. 10, pp. 1507–1516, Oct. 2000.

[13] C.-C. Lu and W. C. Chew, "A multilevel algorithm for solving a boundary integral equation of wave scattering," *Microw. Opt. Technol. Lett.*, vol. 7, no. 10, pp. 466–470, Jul. 1994.

[14] J. Song, C.-C. Lu, and W. Cho Chew, "Multilevel fast multipole algorithm for electromagnetic scattering by large complex objects," *IEEE Trans. Antennas Propag.*, vol. 45, no. 10, pp. 1488–1493, Oct. 1997.

[15] E. Bleszynski, M. Bleszynski, and T. Jaroszewicz, "AIM: Adaptive integral method for solving large-scale electromagnetic scattering and radiation problems," *Radio Sci.*, vol. 31, no. 5, pp. 1225–1251, Sep. 1996.

[16] X. C. Nie, L. W. Li, N. Yuan, T. S. Yeo, and Y. B. Gan, "Precorrected-FFT algorithm for solving combined field integralequations in electromagnetic scattering," *J. Electromag. Waves Appl.*, vol. 16, no. 8, pp. 1171–1187, Jan. 2002.
[17] S. Mo Seo and J.-F. Lee, "A fast IE-FFT algorithm for solving PEC scattering problems," *IEEE Trans. Magn.*, vol. 41, no. 5, pp. 1476–1479, May 2005.
[18] J. R. Phillips and J. K. White, "A precorrected fit method for electrostatic analysis of complicated 3-D structures," *IEEE Trans. Comput.-Aided Design Integr. Circuits Syst.*, vol. 16, no. 10, pp. 1059–1072, Oct. 1997.
[19] X. Nie, L.-W. Li, N. Yuan, and T. S. Yeo, "Fast analysis of scattering by arbitrarily shaped three-dimensional objects using the precorrected-FFT method," *Microw. Opt. Technol. Lett.*, vol. 34, no. 6, pp. 438–442, Sep. 2002.
[20] J. Y. Xie, "Research on fast Fourier transform—Based fast integral equation algorithms," Ph.D. dissertation, Dept. Informt. Sci. Eng., Southeast Univ., Nanjing, China, 2013.
[21] R. J. Burkholder, C. Tokgoz, C. J. Reddy, and W. O. Coburn, "Iterative physical optics for radar scattering predictions," *ACES J.-Appl. Comput. Electromagn. Soc.*, vol. 24, no. 2, p. 241, 2009.
[22] G. H. Golub and C. F. Van Loan, *Matrix Computations*, 3rd ed. Baltimore, MD, USA: The Johns Hopkins Univ. Press, 1996.
[23] S. H. Park, K. K. Park, J. H. Jung, H. T. Kim, and K. T. Kim, "Construction of training database based on high frequency RCS prediction methods for ATR," *J. Electromagn. Waves Appl.*, vol. 22, nos. 5–6, pp. 693–703, Jan. 2008.
[24] R. L. Wagner and W. C. Chew, "A ray-propagation fast multipole algorithm," *Microw. Opt. Technol. Lett.*, vol. 7, no. 10, pp. 435–438, Jul. 1994.
[25] C.-C. Lu and W. C. Chew, "Fast far-field approximation for calculating the RCS of large objects," *Microw. Opt. Technol. Lett.*, vol. 8, no. 5, pp. 238–241, Apr. 1995.
[26] C.-C. Lu, J.-M. Song, W. Cho Chew, and E. Michielssen, "The application of far-field approximation to accelerate the fast multipole method," in *IEEE Antennas Propag. Soc. Int. Symp. Dig.*, Jul. 1996, pp. 1738–1741.
[27] W. Cho Chew, T. Jun Cui, and J. M. Song, "A FAFFA-MLFMA algorithm for electromagnetic scattering," *IEEE Trans. Antennas Propag.*, vol. 50, no. 11, pp. 1641–1649, Nov. 2002.
[28] T. J. Cui, W. C. Chew, and J. M. Song, "Accurate analysis of reflector antennas using FAFFA-MLFMA algorithm," in *Proc. Antennas Appl. Symp.*, Monticello, IL, USA, Oct. 2001, pp. 544–560.
[29] T. J. Cui, W. C. Chew, G. Chen, and J. Song, "Efficient MLFMA, RPFMA, and FAFFA algorithms for EM scattering by very large structures," *IEEE Trans. Antennas Propag.*, vol. 52, no. 3, pp. 759–770, Mar. 2004.
[30] X.-C. Nie, N. Yuan, L.-W. Li, T. S. Yeo, and Y.-B. Gan, "Fast analysis of electromagnetic transmission through arbitrarily shaped airborne radomes using precorrected-FFT method," *Prog. Electromagn. Res.*, vol. 54, pp. 37–59, 2005.
[31] U. Jakobus and F. M. Landstorfer, "Improvement of the PO-MoM hybrid method by accounting for effects of perfectly conducting wedges," *IEEE Trans. Antennas Propag.*, vol. 43, no. 10, pp. 1123–1129, Oct. 1995.
[32] S. Rao, D. Wilton, and A. Glisson, "Electromagnetic scattering by surfaces of arbitrary shape," *IEEE Trans. Antennas Propag.*, vol. AP-30, no. 3, pp. 409–418, May 1982.
[33] R. F. Harrington, *Field Computation by Moments Methods*. New York, NY, USA: Macmillan, 1968.
[34] A. W. Glisson, "Electromagnetic scattering by arbitrarily shaped surfaces with impedance boundary conditions," *Radio Sci.*, vol. 27, no. 6, pp. 935–943, Nov. 1992.
[35] R. J. Burkholder and T. Lundin, "Forward-backward iterative physical optics algorithm for computing the RCS of open-ended cavities," *IEEE Trans. Antennas Propag.*, vol. 53, no. 2, pp. 793–799, Feb. 2005.
[36] J. M. Song and W. C. Chew, "Fast multipole method solution using parametric geometry," *Microw. Opt. Technol. Lett.*, vol. 7, no. 16, pp. 760–765, Nov. 1994.
[37] W. J. Wiscombe, "Improved mie scattering algorithms," *Appl. Opt.*, vol. 19, no. 9, p. 1505, May 1980.
[38] W. Luo, "Research on hybrid fast algorithm for electromagnetic scattering from complex cavities in three-dimensional electric power," Ph.D. dissertation, Electromag. Sci. Technol. China Univ., Anhui, China, 2007.
[39] W. Yang, "Characteristics analysis and modeling research on electromagnetic scattering from 3D complicated rough surface," Ph.D. dissertation, Electromag. Sci. Technol. China Univ., Anhui, China, 2012.
[40] H. X. Ye and Y. Q. Jin, "Parameterization of tapered incident wave for electromagnetic scattering simulation from randomly rough surface," *IEEE Trans. Antennas Propag.*, vol. 53, no. 3, pp. 1234–1237, Mar. 2005.
[41] N. Déchamps, N. de Beaucoudrey, C. Bourlier, and S. Toutain, "Fast numerical method for electromagnetic scattering by rough layered interfaces: Propagation-inside-layer expansion method," *J. Opt. Soc. Amer. A, Opt. Image Sci.*, vol. 23, no. 2, pp. 359–369, 2006.
[42] S. Bellez, C. Bourlier, and G. Kubické, "3-D scattering from a PEC target buried beneath a dielectric rough surface: An efficient PILE-ACA algorithm for solving a hybrid KA-EFIE formulation," *IEEE Trans. Antennas Propag.*, vol. 63, no. 11, pp. 5003–5014, Nov. 2015.
[43] G. Zou, C. Tong, H. Sun, P. Peng, and T. Song, "Analysis of electromagnetic scattering from combined conducting and dielectric objects above rough surface using hybrid SIE-KA-FMM method," *IEEE Access*, vol. 7, pp. 95094–95107, 2019.
[44] G. X. Zou, C. Tong, H. L. Sun, and P. Peng, "Research on electromagnetic scattering characteristics of combined conducting and dielectric target above coastal environment," *IEEE Access*, vol. 8, pp. 169286–169303, 2020.
[45] G. Tian, C. Tong, H. Sun, G. Zou, and H. Liu, "Improved hybrid algorithm for composite scattering from multiple 3D objects above a 2D random dielectric rough surface," *IEEE Access*, vol. 9, pp. 4435–4446, 2021.

GUILONG TIAN was born in Hunan, China, in 1994. He received the B.S. degree in electronics science and technology, in 2012, and the M.S. degree in electromagnetic theory and engineering from Air Force Engineering University, Xi'an, China, in 2016, where he is currently pursuing the Ph.D. degree in electronics science and technology. His research interests include computational electromagnetics and composite scattering from objects above rough surface.

CHUANGMING TONG was a Visiting Scientist Postdoctoral Fellow with Southeast University, Nanjing, China. He is currently a Professor with the Department of Electronics and Communication Engineering, Air and Missile Defense College, Air Force Engineering University. He has more than 20 years of experience in teaching and research. His research interests include microwave remote sensing, electromagnetic waves, polarimetric and interferometric applications of microwave data, numerical modeling, and ground penetrating radar through wall imaging and stealth technology. He received various fellowships and awards from national and international bodies.

TONG WANG received the B.S. degree in electromagnetic wave propagation and antenna and the M.S and Ph.D. degrees in electromagnetic field and microwave technology from Air Force Engineering University, Xi'an, China, in 2012, 2014, and 2018, respectively. He is currently a Lecturer with the School of Air and Missile Defense, Air Force Engineering University. His current research interests include computational electromagnetics, wave scattering from rough surface, radar raw signals simulation, and synthetic aperture radar (SAR) image interpretation.

DONGLI TANG received the B.S. degree in measurement and control engineering and the M.S degree in navigation, guidance, and control from Air Force Engineering University, Xi'an, China, in 2008 and 2010, respectively.

He is currently a Lecturer with the School of Air and Missile Defense, Air Force Engineering University. His current research interests include education management and computational electromagnetics.